# Influence of a Rapidly Uplifting Orogen on the Preservation of Climate Oscillations

**Amy I. Hsieh[1,2]** [ID], **Romain Vaucher[3,4]** [ID], **Ludvig Löwemark[2,5]** [ID], **Shahin E. Dashtgard[1]** [ID], **Chorng-Shern Horng[6]** [ID], **Andrew T. Lin[7]** [ID], and **Christian Zeeden[8]** [ID]

[1]Department of Earth Sciences, Paleoclimate Records in Shallow Marine Strata (PRISMS) Research Group, Simon Fraser University, Burnaby, BC, Canada, [2]Department of Geosciences, National Taiwan University, Taipei, Taiwan, [3]Institute of Earth Sciences (ISTE), University of Lausanne, Lausanne, Switzerland, [4]Department of Earth Sciences, University of Geneva, Geneva, Switzerland, [5]Research Center for Future Earth, National Taiwan University, Taipei, Taiwan, [6]Institute of Earth Sciences, Academia Sinica, Taipei, Taiwan, [7]Department of Earth Sciences, National Central University, Taoyuan, Taiwan, [8]Leibniz Institute for Applied Geophysics (LIAG), Geozentrum Hannover, Hannover, Germany

**Abstract** Climate oscillations preserved in sedimentary archives tend to decrease in resolution further back in Earth's history. High-frequency climate cycles (e.g., ~20-Kyr precession cycles) are especially prone to poor preservation due to sediment reworking. Recent studies have shown, however, that given sufficient basin accommodation space and sedimentation rate, shallow-marine paleoclimate archives record precession-driven hydroclimate change in mid-low latitude regions. Our study evaluates how the evolution of a rapidly uplifting orogen influences the recording of astronomical climate forcing in shallow-marine sedimentary strata in the Taiwan Western Foreland Basin (WFB). Time-series analysis of gamma-ray records through the late Miocene–Pliocene Kueichulin Formation shows that during early stages of Taiwan orogenesis (before 5.4 Ma), preservation of precession-driven East Asian Summer Monsoon variability is low despite increasing monsoon intensities between 8 and 3 Ma. The Taiwan Strait had not formed, and the southeast margin of Eurasia was open to the Pacific Ocean. Consequently, depositional environments in the WFB were susceptible to reworking by large waves, resulting in the obscuration of higher-frequency precession cycles. From 5.4 to 4.92 Ma, during early stages of emergence of Taiwan, basin subsidence increased while sedimentation rates remained low, resulting in poor preservation of orbital oscillations. After 4.92 Ma and up to 3.15 Ma, Taiwan became a major sediment source to the WFB, and sheltered the WFB from erosive waves with the development of Taiwan Strait. The elevated sediment influx, increased basin accommodation as the WFB developed, and formation of a semi-sheltered strait, resulted in enhanced preservation of precession-driven East Asian Summer Monsoon variability.

**Plain Language Summary** Rhythmic changes in the shape of Earth's orbit (eccentricity, ~100-Kyr cycles), tilt (obliquity, ~41-Kyr cycles), and axial rotation (precession, ~20-Kyr cycles) drive climate change that may be preserved in sedimentary records. Orbital climate cycles are recorded in clastic shallow-marine strata where the amount of sediment transported from land to sea and space available for deposition in the basin are sufficiently high. Our study of the Kueichulin Formation in the Taiwan Western Foreland Basin (WFB) shows how a rapidly uplifting orogen influences the preservation of different climate cycles in the shallow-marine realm. During early Taiwan orogenesis (before 5.4 Ma) when the Taiwan Strait did not exist, sediment in the WFB were susceptible to reworking by erosive waves generated in the Pacific Ocean, which obscured higher-frequency precession cycles. From 5.4 to 4.92 Ma, Taiwan began to emerge from the Pacific Ocean and the WFB began to subside, but sedimentation rates were low, so climate cycles were poorly preserved. After 4.92 Ma, rapid uplift and erosion of Taiwan and WFB subsidence continued, resulting in increased sedimentation to the sea, increased sediment accumulation space, and the formation of a strait that sheltered the WFB from waves, which all served to enhance the preservation of precession.

## 1. Introduction

The Pliocene Epoch (from 5.33 to 2.58 Ma) is the most recent time in Earth's history prior to the pre-industrial period during which atmospheric $CO_2$ concentrations exceeded 400 ppm (Burke et al., 2018; Haywood et al., 2013; Keeling & Keeling, 2017; Raymo & Horowitz, 1996; Tierney et al., 2019). Estimates suggest that global temperatures during the mid-Pliocene Warm Period were as much as 3°C higher than the pre-industrial period (Haywood

**Validation:** Romain Vaucher, Ludvig Löwemark, Shahin E. Dashtgard, Christian Zeeden
**Writing – original draft:** Amy I. Hsieh
**Writing – review & editing:** Amy I. Hsieh, Romain Vaucher, Ludvig Löwemark, Shahin E. Dashtgard, Chorng-Shern Horng, Andrew T. Lin, Christian Zeeden

et al., 2013; Haywood & Valdes, 2004). Polar ice volumes are hypothesized to have been reduced during the mid-Pliocene under permanent, El Niño-like conditions (Dekens et al., 2007; Dolan et al., 2011; Dowsett et al., 2012; Fedorov et al., 2006, 2010, 2013; Haywood et al., 2013; Hill et al., 2010; Lunt et al., 2008; Naish et al., 2009; Pollard & DeConto, 2009; Wara et al., 2005), and sea level was $22 \pm 10$ m higher than the present day (Dowsett & Cronin, 1990; Haywood et al., 2013; Miller et al., 2012). The changes in sea-surface temperatures and polar ice volumes resulted in East Asian Summer Monsoon (EASM) variations, and probably also considerably more intense and frequent tropical cyclones than the present-day (Coumou & Rahmstorf, 2012; Fedorov et al., 2010; Gai et al., 2020; Kelman, 2013; Kossin, 2018; Kossin et al., 2020; Yan et al., 2016). Consequently, the Pliocene Earth system provides a possible analogue for understanding future climate-induced environmental changes (Burke et al., 2018; Raymo & Horowitz, 1996; Tierney et al., 2019).

Late Miocene to Pliocene climate reconstructions have emphasized the influence of 41-Kyr glacial and interglacial cycles on temperature, ice volume, and the hydrologic cycle on a global scale because obliquity is the dominant signal preserved in many geologic records from that time (e.g., Clement et al., 2004; Naish et al., 2009; Patterson et al., 2014). This relationship may not be applicable in mid-low latitude regions, however, because at these latitudes the hydrological processes that control sediment flux from land to sea are largely independent of glacial-interglacial cycles and instead are predominantly controlled by summer insolation which respond to eccentricity-modulated precession (Berger et al., 2006; Clement et al., 2004; Gai et al., 2020; Kutzbach, 1981; Prell & Kutzbach, 1987; Tachikawa et al., 2011; Wang et al., 2017; Yamamoto et al., 2013). Indeed, EASM records from the Chinese Loess Plateau show strong precession signals (Ao et al., 2016, 2021; Sun et al., 2010; S. Yang et al., 2018) while precession signals tend to be obscured by obliquity in time-equivalent deep-sea marine proxies, especially those from the South China Sea (Ao et al., 2011, 2016, 2021; Gai et al., 2020; Holbourn et al., 2021; Huybers, 2006; Li & Wang, 2015; Shi et al., 2022; Wang et al., 2017; Zhang et al., 2022). Shallow-marine environments are directly affected by processes related to climate change, such as sea-level fluctuations and extreme weather events, and have been shown to preserve precession cycles where sedimentation rates and accommodation space creation are sufficiently high (Grant et al., 2019; Vaucher et al., 2021; Vaucher, Zeeden, et al., 2023).

In this study, we (a) assess the influence of a rapidly uplift orogen on the preservation of climate oscillations, and (b) identify changes in orbital periodicities preserved in sedimentary archives that reflect different stages of Taiwan orogenesis. This is done by analyzing late Miocene–Pliocene gamma-ray (GR) records from the Kueichulin Formation in the Western Foreland Basin (WFB), Taiwan.
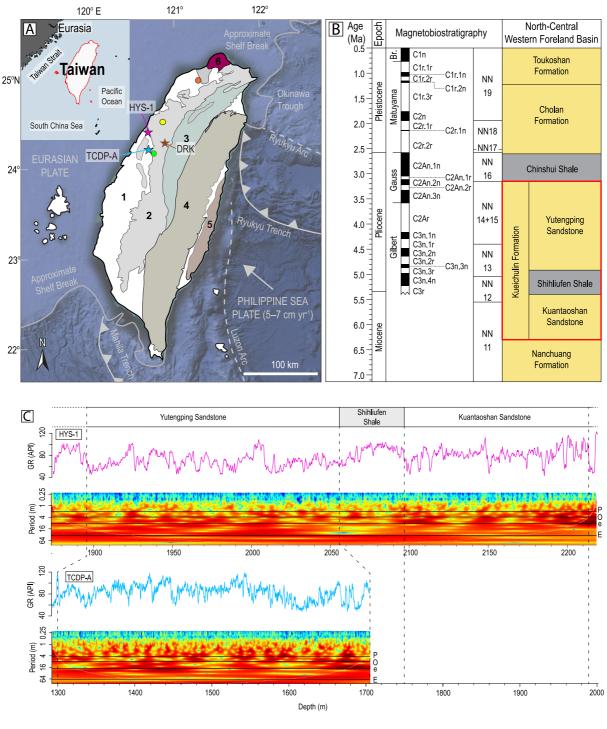
## 2. Geologic Setting

The Taiwan orogenic belt was formed through the collision of the Luzon Arc on the Philippine Sea Plate and the Eurasian Plate, and this began in the late Miocene (Castelltort et al., 2011; Covey, 1986; A. T. Lin et al., 2003; A. T. Lin & Watts, 2002; Nagel et al., 2018; Pan et al., 2015). The collision propagated to the south, and triggered lithospheric flexure of the Eurasian Plate and formation of the WFB (Castelltort et al., 2011; Y.-W. Chou & Yu, 2002; Covey, 1986; A. T. Lin & Watts, 2002; Simoes & Avouac, 2006; Teng, 1990; Yu & Chou, 2001). Late Miocene to Pleistocene sedimentary strata in the WFB comprise thick sequences of shelfal through terrestrial sediments (A. T. Lin & Watts, 2002; Yu & Chou, 2001).

This study focuses on the late Miocene to early Pliocene Kueichulin Formation (Fm; Figures 1a and 1b), which was deposited during the early stages of Luzon Arc-Eurasian Plate collision. The Kueichulin Fm is selected for this study because it comprises (quasi) continuous shallow marine strata that were directly affected by climate-related sea-level fluctuations and extreme weather events (Covey, 1986; Dashtgard et al., 2020, 2021; Hsieh et al., 2022; Nagel et al., 2013, 2014). Recent studies by Vaucher et al. (2021) and Vaucher, Zeeden, et al. (2023) showed that high-resolution climate signals were preserved in lower Pleistocene shallow-marine strata of the WFB due to high accommodation and high sedimentation rates in the basin. In turn, the sedimentation rate and accommodation space of the WFB during the deposition of the Kueichulin Fm should have been sufficiently high, in theory, increasing the likelihood of preserving climate signals.

The Kueichulin Fm is recognized across the north-central WFB and comprises mainly shallow-marine and deltaic strata deposited between 10 and >35 m water depths (Castelltort et al., 2011; Covey, 1986; Dashtgard et al., 2020, 2021; A. T. Lin et al., 2003; Nagel et al., 2013; Pan et al., 2015; Yu & Chou, 2001) and is divided into three members (from bottom to top): Kuantaoshan Sandstone, Shihliufen Shale, and Yutengping Sandstone

**Figure 1.**

(Figure 1b; Castelltort et al., 2011; A. T. Lin et al., 2007; Pan et al., 2015; Shaw, 1996). A recent study by Hsieh et al. (2022) using a combination of clay mineralogy, $\delta^{13}C_{org}$ and C/N of organic matter, and mass-specific magnetic susceptibility records from the Kueichulin Fm shows that the Taiwan orogen became a major sediment source to the WFB shortly after its emergence due to its rapid rate of uplift and erosion.

The Kuantaoshan Sandstone consists of hummocky cross-stratified sandstone with low bioturbation intensities and scour-and-fill structures. The Shihliufen Shale comprises mudstone deposited in a fully marine, offshore

environment (Castelltort et al., 2011; Chang, 1971; Dashtgard et al., 2021; Nagel et al., 2013), and the Yutengping Sandstone comprises sandy mudstone, muddy sandstone, and sandstone with varying intensities of bioturbation (Castelltort et al., 2011; Dashtgard et al., 2020, 2021; A. T. Lin et al., 2007; Nagel et al., 2013). The Kueichulin Fm is underlain by the Nanchuang Fm, which comprises tidally influenced shallow marine sediments (Castelltort et al., 2011; J. T. Chou, 1972; A. T. Lin et al., 2003; Nagel et al., 2013; Pan et al., 2015). Overlying the Kueichulin Fm is the late Pliocene Chinshui Shale, composed of mudstone deposited in an offshore environment during a period of maximum flooding in the WFB (Castelltort et al., 2011; Nagel et al., 2013, 2018; Pan et al., 2015). The early Pleistocene Cholan Fm is composed of heterolithic, shallow-marine strata, and at the top of the succession is the Toukoshan Fm, which comprises mainly terrestrial conglomerates (Covey, 1986; Nagel et al., 2013; Pan et al., 2015; Vaucher et al., 2021).

## 3. Methodology

### 3.1. Gamma-Ray Data

Gamma-ray data are from two boreholes drilled in the WFB: HYS-1 and TCDP-A (see, Hsieh et al. (2023) for gamma ray data, and A. T. Lin et al. (2007) for core descriptions and geologic maps; Figures 1a and 1c). Variations in GR intensity correspond largely to changes in lithology (Green & Fearon, 1940; Schlumberger, 1989) Generally, in siliciclastic sedimentary strata, GR values below 75 American Petroleum Institute (API) units correspond to intervals dominated by sandstone and in rare cases, conglomerate, and high GR values, above 105 API, indicate high proportions of mudstone which are enriched with radiogenic minerals. Gamma-ray values between 75 and 105 API correspond to heterolithic units or muddy sandstone/sandy mudstone. The Kueichulin Fm is characterized by high proportions of sandstone with GR values less than 75 API. GR data from HYS-1 extend through the entire Kueichulin Fm from a depth of 2,213 m–1,894 m. Data from TCDP-A are only available for the Yutengping Sandstone from a depth of 1,707–1,300 m. The base of the Yutengping Sandstone in TCDP-A is delineated by the Sanyi Fault, which thrust the Kueichulin Fm atop the younger Cholan Fm (A. T. Lin et al., 2007).

### 3.2. Magnetobiostratigraphic Analysis

The chronostratigraphy of the Kueichulin Fm is based on magnetobiostratigraphy. Paleomagnetic oriented cores (25-mm in diameter) were collected on average every 6.4 m vertically from 66 unweathered, mud-rich beds at an outcrop of the formation along the Da'an River (Figure 1a, see also Figure S1 in Supporting Information S1). Core samples were acquired from the upper Kuantaoshan Sandstone, the Shihliufen Shale, and upwards through the lower-middle Yutengping Sandstone; these samples were analyzed for their magnetic remanent directions. In each unweathered, mud-rich bed, 2–3 core samples were collected, and the azimuth and dip of each core were measured using an orientation tool with a magnetic compass. Cores were cut into 2-cm lengths, and a JR-6A spinner magnetometer (AGICO) at Academia Sinica in Taiwan was used to obtain the remanent magnetic intensity, and declination and inclination of samples. The samples were then thermally demagnetized in steps from 25 to 600°C to remove unstable secondary magnetization and determine stable remanent magnetization and polarity (i.e., normal or reversed). The magnetic susceptibility of each sample was measured after each demagnetizing step using a MS2B system (Bartington Instruments) to assess changes in magnetic minerals. After completion of thermal demagnetization, the characteristic remanent magnetization (ChRM) declination and inclination were calculated in the PuffinPlot software (Lurcock & Wilson, 2012) using principal component analysis to determine the polarity of the sample using a minimum of four demagnetization steps (Figure S2 in

**Figure 1.** (a) Simplified geological map of Taiwan, showing the main geologic provinces: Coastal Plain and Terraces (1), Western Foothills (2), Hsueshan Range (3), Central Range (4), Coastal Range (5), and Tatun Volcano Group (6) (data from A. T. Lin et al., 2003; C.-W. Lin & Chen, 2016; Simoes & Avouac, 2006). The inset map shows the geographical location of Taiwan. The location of the HYS-1 borehole is marked by the pink star (120.702024°E, 24.399908°N) and the blue star marks the TCDP-A borehole (120.73916°E, 24.20083°N). The Da'an River, Kueichulin Fm outcrop (DRK: 120.91062°E, 24.29479°N) is shown by the brown star. Circles indicate locations of stratigraphic sections used to assess foreland basin subsidence: Dahan River (orange), Chuhuangkeng (yellow), and Tsaohu River (green) (from Nagel et al., 2013) (background image source: Google Earth). (b) Geochronology of sedimentary strata in north-central parts of the WFB of Taiwan (after Teng et al. (1991) and Chen (2016)). The Kueichulin Fm is highlighted in the red box. Yellow denotes that the main lithology is sandstone and gray indicates shale. Paleomagnetic polarity reversals and nannofossil zonations (NN) are also shown (Horng & Shea, 2007; Pan et al., 2015; Vaucher et al., 2021; Vaucher, Zeeden, et al., 2023). Magnetostratigraphic polarity unit Br. = Brunhes, $n$ = normal polarity, and $r$ = reversed polarity. (c) True vertical depth, gamma-ray profiles and wavelet analysis of data from HYS-1 and TCDP-A. Periods of orbital parameters were estimated for HYS-1 and TCDP-A in the depth domain using linear sedimentation rates calculated from magnetobiostratigraphic age boundaries. $P$ = precession (~2 m for HYS-1, ~7 m for TCDP-A), $O$ = obliquity (~4 m for HYS-1, ~13 m for TCDP-A), $e$ = short eccentricity (~10 m for HYS-1, ~31 m for TCDP-A), and $E$ = long eccentricity (~40 m for HYS-1, ~126 m for TCDP-A).

Supporting Information S1). Thermal demagnetization diagrams for nine representative samples from the Da'an River outcrop showing the stable remanent magnetic declinations and inclinations after principal component analysis are presented in Figure S3 in Supporting Information S1.

Thin section slides were prepared for each sample using offcuts of the cores and were examined for calcareous nannofossils using a 1000x magnification optical microscope. Index nannofossils and their corresponding biozonations were identified to constrain paleomagnetic polarities and to determine the ages of strata in the Kueichulin Fm (Chang & Chi, 1983; Huang, 1976; Martini, 1971; Raffi et al., 2006; Shea & Huang, 2003).

The stratigraphic boundaries between members of the Kueichulin Fm were identified along the Da'an River outcrop based on sedimentological and ichnological characteristics (see Hsieh et al., 2022). The magnetobiostratigraphic ages of these boundaries were then correlated from the outcrop section to the HYS-1 and TCDP-A boreholes based on the stratigraphic boundaries identified by A. T. Lin et al. (2007). Due to the regional extent of the Kueichulin Fm across the north-central WFB and the overall similarity of GR patterns between HYS-1 and TCDP-A, we assume no diachroneity across the stratigraphic units.
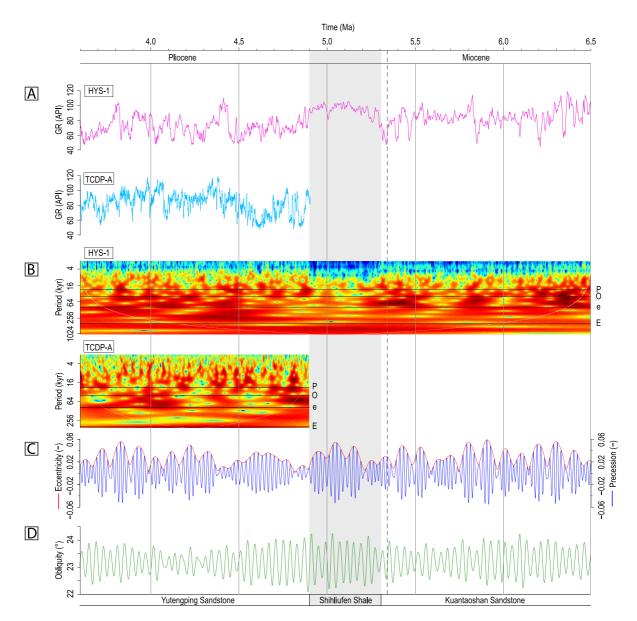
### 3.3. Time-Series Analysis

To detect the main cyclic components preserved in the GR records, we conducted wavelet analysis using the "biwavelet" R package (Gouhier et al., 2018). This is done, because power spectra integrate over a large depth range with possibly changing sedimentation rate in this case. The results are then compared to eccentricity, obliquity, and precession to resolve orbital forcing on the sedimentary system. Using magnetobiostratigraphic age boundaries, we estimated linear sedimentation rates for the Kueichulin Fm of 0.01 m/Kyr at HYS-1, and the Yutengping Sandstone of 0.31 m/Kyr at TCDP-A (Table S1 in Supporting Information S1). Using the estimated linear sedimentation rates, we calculated periods for eccentricity, obliquity, and precession in the depth domain. Wavelet analyses of the GR data in the depth domain is compared at periods of 40, 10, 4, and 2 m for HYS-1, and 126, 31, 13, and 7 m for TCDP-A, which represent long-eccentricity, short-eccentricity, obliquity, and precession cycles, respectively (Figure 1c). Wavelet analysis was also conducted on the GR data tied to magnetobiostratigraphic age boundaries to determine if orbital cycles exist within our datasets (Figure 2). Overall, the results of wavelet analyses in both the depth domain and magnetobiostratigraphic time domain at both sites displayed strong signals that match expected orbital periods. This suggests that an astronomical forcing exists in both GR records.

Variations in GR are correlated to an orbitally tuned, benthic foraminiferal, stable oxygen isotope ($\delta^{18}$O) record from the equatorial Atlantic Ocean (Wilkens et al., 2017; Figure 3a). The $\delta^{18}$O record represents mainly global ice volume, which drives sea level. The correlation between the GR records and the $\delta^{18}$O record is based on the assumption that chemical weathering is enhanced under warm, humid climates (i.e., when sea level is high). The production of mud- and clay-rich sediment increases with temperature and humidity (Brady & Weil, 2017; Singer, 1980) and the export of mud from land increases through enhanced precipitation as a result of increased EASM and tropical cyclone activity (Dadson et al., 2004; Milliman et al., 2007; Milliman & Kao, 2005). In contrast, physical weathering is enhanced under global cool, dry climates, which correspond to sea-level lowstands. Cool, dry climates are times when sand-rich sediments are transported farther into sedimentary basins due to lower sea levels (Catuneanu, 2006).

The GR records were tuned to the $\delta^{18}$O record of Wilkens et al. (2017) based on the assumption that intervals of low GR values (i.e., sandstone-rich) correlate to $\delta^{18}$O maxima, while intervals of high GR values (i.e., mudstone-rich) correlate to $\delta^{18}$O minima. The $\delta^{18}$O record of Wilkens et al. (2017) is used for orbital tuning because it was tuned to physical sedimentary properties independent of ice volume, and has a robust timescale. Because of the global signature of the $\delta^{18}$O signal, a proximal (local) reference record is not needed. Magnetobiostratigraphic age boundaries defined in the Kueichulin Fm are used to constrain the tie points used to tune the GR records to the benthic foraminiferal $\delta^{18}$O record. Variations in benthic foraminiferal $\delta^{18}$O values are related to changes in global ice volume and deep-sea temperatures, high $\delta^{18}$O values correspond to periods of cooling and glaciation (i.e., sea level minima), and low $\delta^{18}$O values correspond to warm, interglacial periods (i.e., sea level maxima) (Savin et al., 1975).

Time-series and astrochronological analyses were completed using the open-source software "R" and the "astrochron" package (Meyers, 2014; R Core Team, 2022). The "testTilt" (Zeeden et al., 2019) and "testPrecession"
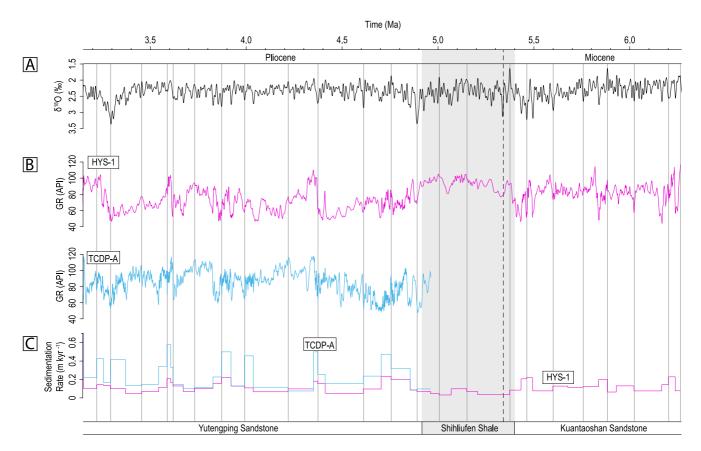
**Figure 2.** (a) Gamma-ray data from HYS-1 and TCDP-A correlated to magnetobiostratigraphic age boundaries for the Kuantaoshan Sandstone, the Shihliufen Shale, and the Yutengping Sandstone. (b) Results of wavelet analyses for HYS-1 and TCDP-A. The *y*-axes represent the periodicity of orbital cycles, where $P$ = precession (20-Kyr periodicity), $O$ = obliquity (41-Kyr periodicity), $e$ = short eccentricity (100-Kyr periodicity), and $E$ = long eccentricity (405-Kyr periodicity). Blue and green colors in the wavelet analyses indicate time intervals of no or little cyclicity in the GR record at a specific period, and red and yellow colors indicate intervals of strong cyclicity. (c) Astronomical solution of Earth's eccentricity (red) and precession (blue) and (d) obliquity for the studied time interval (Laskar et al., 2004) used for comparison with the sedimentary record as shown using wavelet analysis in (b). The black dashed line indicates the Miocene-Pliocene transition.

(Meyers, 2014; Zeeden et al., 2015) functions were used to test for obliquity and eccentricity-modulated precession amplitudes in the GR data sets and to compare them to theoretical orbital obliquity and precession. This methodology tests the integrity of the tuning results while accounting for possible frequency modulation of the tuning process. Power spectra for the GR records are also calculated using the multitaper method for spectral analysis (Meyers, 2012; Thomson, 1982) to identify prominent orbital cycles within the record (Figure S5 in Supporting Information S1). The tuning tie points are available in Table S2 in Supporting Information S1, and the R script is available in Hsieh et al. (2023).

To evaluate the individual effect of eccentricity, obliquity, and precession forcing, we filter the GR data using a Taner bandpass filter at different periodicities (Taner, 1992). We apply low-frequency and high-frequency cut-off-frequencies of 0.0125 cycle Kyr$^{-1}$ and 0.007 cycle Kyr$^{-1}$ for eccentricity, 0.03 cycle Kyr$^{-1}$ and 0.021

**Figure 3.** (a) Benthic foraminiferal δ^18O record (Wilkens et al., 2017) used to tune the GR records. (b) Astronomically tuned and correlated GR data from HYS-1 and TCDP-A (A. T. Lin et al., 2007). Select tie points used to tune the data sets are shown by vertical gray lines. Please refer to Table S2 in Supporting Information S1 for all tie points used. (c) Sedimentation rates calculated for HYS-1 and TCDP-A. The vertical black dashed line marks the Miocene-Pliocene transition.

cycle Kyr$^{-1}$ for obliquity, and 0.06 cycle Kyr$^{-1}$ and 0.04 cycle Kyr$^{-1}$ for precession, respectively (Zeeden et al., 2018). Instantaneous amplitudes for each record are determined with a Hilbert transform to isolate the amplitudes of eccentricity, obliquity, or precession-frequency components. This allows for the comparison of individual orbital components preserved in the record against calculations of orbital indices by Laskar et al. (2004), as shown in Figures 2c and 2d.

## 4. Results

### 4.1. Age Model

Paleomagnetic samples collected from the Kueichulin Fm outcrop along the Da'an River preserve a magnetic polarity sequence, and when combined with index nannofossil zonations, provide high-resolution age constraints for the Shihliufen Shale and Yutengping Sandstone (Figure 1b; see also Figure S4 in Supporting Information S1 and Hsieh et al., 2023 for magnetobiostratigraphic data). Magnetic polarities could not be determined for the Kuantaoshan Sandstone due to its coarse grain size, resulting in unstable remanent magnetization during thermal demagnetization; however, based on the presence of the index nannofossils *Discoaster quinqueramus* and *Triquetrorhabdulus rugosus*, it belongs to nannofossil zonations of NN11–NN12 (Raffi et al., 2020). The Shihliufen Shale shows a reversed-normal-reversed polarity sequence upwards, and the presence of *Ceratolithus acutus* and *Ceratolithus rugosus* (NN12–NN13; Raffi et al., 2020) assign the magnetic polarities to the lower Gilbert chron (C3r, C3n.4n, and C3n.3r, respectively; Ogg, 2020) across the Miocene/Pliocene boundary (Figure 1b; see Hsieh et al., 2023 for magnetobiostratigraphic data). Samples collected from the lower-middle Yutengping Sandstone interval show three normal magnetic polarities intercalated with reversed polarities, which are constrained to the mid-to upper-Gilbert chron (from C3n.3r to C2Ar; Figure 1b; see Hsieh et al., 2023) by the presence of large form (~7 mm in diameter) of *Reticulofenestra pseudoumbilicus* and *Sphenolithus abies* (NN13–NN14;

Ogg, 2020; Raffi et al., 2020). This suggests that the boundary between the Kuantaoshan Sandstone and the overlying Shihliufen Shale occurred near the Miocene-Pliocene transition at ca. 5.3 Ma, and the boundary between the Shihliufen Shale and Yutengping Sandstone boundary occurred near 4.92 Ma (Hsieh et al., 2022). A study by Horng and Shea (2007) based on magnetic polarity records of Taiwan of the Pliocene-Pleistocene shows that the base of the Chinshui Shale (i.e., the top of the Yutengping Sandstone) occurs near the Gilbert-Gauss polarity boundary at 3.6 Ma. The magnetobiostratigraphic ages are then used to tune the GR data to the $\delta^{18}O$ record with tie points (see Supplementary Materials 1 and 3 in Supporting Information S1) to construct an age model for the two boreholes (Figures 3a and 3b). The tuned age model shows that the upper part of the Kuantaoshan Sandstone was deposited between ca. 6.27 and 5.4 Ma, the Shihliufen Shale between ca. 5.4 and 4.92 Ma, and the Yutengping Sandstone between ca. 4.92 and 3.15 Ma (Figures 3a and 3b).

While uncertainties remain in the magnetobiostratigraphic age constraints due to unstable remanent magnetization and the presence and preservation of index nannofossils, especially in the coarser-grained Kuantaoshan Sandstone and Yutengping Sandstone, the magnetobiostratigraphic age of the Shihliufen Shale appears robust (i.e., the ages of the boundaries between each member of the Kueichulin Fm are constrained). In addition, our magnetobiostratigraphic age data are supported by existing magnetobiostratigraphy for the Kueichulin Fm.

Sedimentation rates through the Kueichulin Fm are calculated based on our integrated age model (Figure 3c). The results show that sedimentation recorded in both the HYS-1 and TCDP-A wellbores and over similar intervals, fluctuated between multiple phases of low rates followed by high rates. Sedimentation rates in the Kuantaoshan Sandstone range from 0.06 to 0.23 m Kyr$^{-1}$ (average 0.13 m Kyr$^{-1}$). Sedimentation rates are lowest in the Shihliufen Shale, ranging from 0.03 to 0.10 m Kyr$^{-1}$ (average 0.06 m Kyr$^{-1}$). In the Yutengping Sandstone, sedimentation rates are higher in TCDP-A (average 0.26 m Kyr$^{-1}$) and the range of values are more extreme (0.08–0.58 m Kyr$^{-1}$) compared to HYS-1 (0.05–0.24 m Kyr$^{-1}$; average 0.12 m Kyr$^{-1}$). An anomalously high sedimentation rate of 0.7 m Kyr$^{-1}$ at 3.15 Ma in both the HYS-1 and TCDP-A is probably the result of an edge effect caused by the age boundary imposed at the top of the GR data sets and is not deemed to reflect actual sedimentation rates. Consequently, the anomalous sedimentation rate is excluded in the calculation of average rates.

Results from the "testTilt" function (Figure 4a) show that the match between obliquity amplitudes and the GR datasets is poor for HYS-1 and strong for TCDP-A. Results from the "testPrecession" function (Figure 4b) show that the match between precession amplitudes and the HYS-1 GR data is poor. The match between precession amplitudes and TCDP-A GR data is highest when orbital eccentricity amplitudes are high (i.e., after 4 Ma), and this is expected because the precession signal is typically poorly preserved in geologic records during low eccentricity. The older limits are different for the time periods tested for obliquity and precession amplitude modulation because of the different age ranges of the GR records (i.e., HYS-1 extends from 6.27 Ma to 3.15 Ma, while TCDP-A only extends from 5 Ma to 3.15 Ma). Therefore, the orbital data processed for obliquity and precession are slightly different for both HYS-1 and TCDP-A.
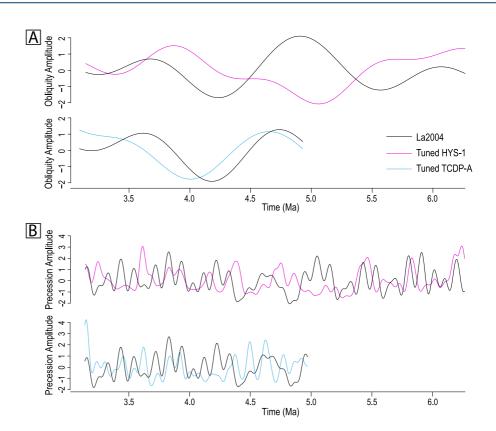
## 4.2. Time-Series Analysis and Orbital Imprint

Results of wavelet analysis show that the Kueichulin Fm GR record in both the HYS-1 and TCDP-A boreholes (Figure 5a) preserves evidence of both long- and short-eccentricity, obliquity, and precession cycles. Through the Kueichulin Fm there is a strong signal at the 405-Kyr period in both HYS-1 and TCDP-A, and this corresponds to long eccentricity, with the maximum occurring in the Yutengping Sandstone (Figure 5b). Through the Kuantaoshan Sandstone and lower Shihliufen Shale (6.27–5.3 Ma), 100- and 41-Kyr cycles are most prevalent. The strong, 100-Kyr period signal across this time interval corresponds with high eccentricity, with maxima near 5.8 Ma and 5.4 Ma, and a minimum near 5.7 Ma (Figures 5b and 5c). For the 41-Kyr period, the signal is strongest when eccentricity and precession are at a minimum, with the strongest signals appearing near 5.9 Ma and 5.5 Ma (Figures 5b–5d). Cycles with a 20-Kyr periodicity exhibit higher variability through the 6.27–5.3 Ma interval (Figures 5b and 5c). The influence of orbital obliquity and precession on the GR record appears to diminish abruptly through the middle to upper Shihliufen Shale (5.3–4.92 Ma), while eccentricity shows a slight weakening (Figure 5b). Through the Yutengping Sandstone, the 100-Kyr signal remains clear and rather constant in the HYS-1 borehole, while the GR record in the TCDP-A borehole shows variations in the signal strength that correspond to increasing and decreasing eccentricity influence (Figure 5b). The 41-Kyr signal increases in strength again in strata younger than 5 Ma and appears stronger in the HYS-1 record than in the TCDP-A record (Figure 5b). In HYS-1, 20-Kyr cycles are strongest during eccentricity and precession minima, while in TCDP-A the strongest signals correspond to precession maxima (Figures 5b and 5c).
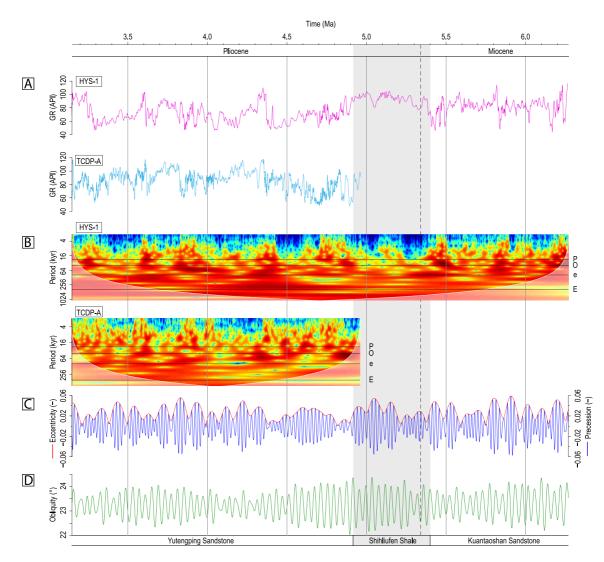
**Figure 4.** Results of the (a) "TestTilt" and (b) "TestPrecession"" functions for tuned GR data of TCDP-A and HYS-1. These tests assess the robustness of astronomical tuning against astronomical solutions of orbital indices (La2004; Laskar et al., 2004). The mismatch between obliquity and precession and the La2004 astronomical solutions in both records is probably due to a lack of a dominant signal in the record.

The filtered GR data show elevated amplitudes at 41-Kyr cycles preserved at both HYS-1 and TCDP-A (Figures 6a and 6b). However, amplitudes are generally low except during obliquity maxima and/or eccentricity minima (i.e., near 5.5, 4.9, and 3.6 Ma). Obliquity amplitudes are also low through the Shihliufen Shale, despite increasing orbital obliquity. Short eccentricity is pervasive throughout the Kueichulin Fm, with variations in the 100-Kyr amplitudes corresponding well with eccentricity (i.e., maxima near 5.4, 5.1, and 3.7 Ma; Figures 6c and 6d), except in the Shihliufen Shale where 100-Kyr amplitudes are low despite an eccentricity maximum. While 20-Kyr cycles are expressed in the GR data, they are obscured by the stronger, lower-frequency cycles (i.e., ≥41-Kyr cycles) in the wavelet analysis (Figure 5b). After removal of the lower-frequency cycles by applying the Taner filter, the 20-Kyr signal and its variations are more clearly expressed in the GR records (Figure 6e). Through the Kuantaoshan Sandstone, the relative amplitudes (i.e., strength) of 20-Kyr cycles are low and not highly variable except near both the base of the Kuantaoshan Sandstone and near the Shihliufen Shale-Kuantaoshan Sandstone boundary (ca. 6.2 Ma and 5.4 Ma, respectively); both of these stratal intervals record eccentricity maxima and obliquity minima. The 20-Kyr signal decreases to a minimum through the Shihliufen Shale despite high and variable precession (Figure 6c). Through the Yutengping Sandstone, the amplitude of the 20-Kyr signal is at a maximum, and peaks in 20-Kyr cycles generally correspond to precession maxima (i.e., near 5.4, 4.6, and 3.6 Ma); this is expressed more clearly in TCDP-A (Figure 6e).

## 5. Discussion

Presently, sediment is transported from the Taiwan orogen to the Taiwan Strait primarily during high precipitation and runoff associated with the EASM and tropical cyclones (C.-W. Chen et al., 2018; Dadson et al., 2003, 2004; Dashtgard et al., 2021; Kao & Milliman, 2008; Milliman et al., 2007, 2017; Milliman & Kao, 2005; Steer et al., 2020; Vaucher et al., 2021; Vaucher, Zeeden, et al., 2023; Y. Yang et al., 2022). Sediment transport was likely similar in the geologic past because the morphology, tectonic setting, and evolution of Taiwan have remained
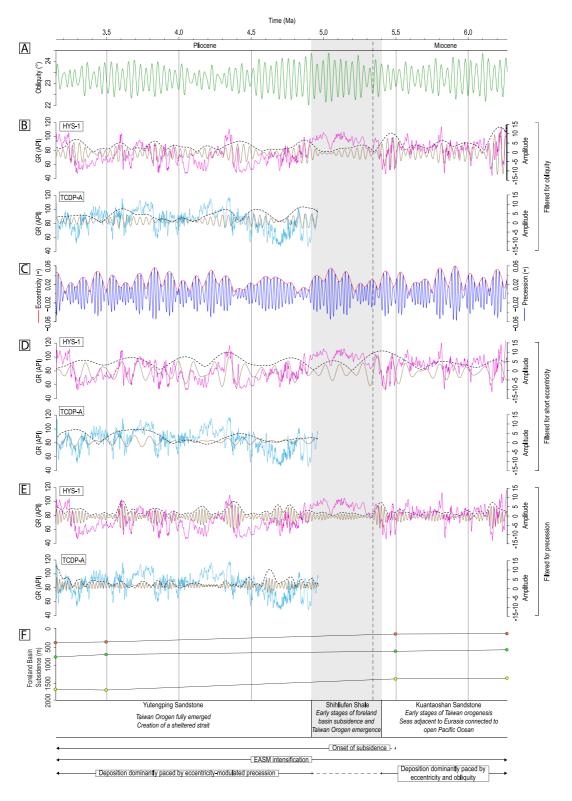
**Figure 5.** (a) Correlated gamma-ray data from HYS-1 and TCDP-A tuned to the δ18O record from Wilkens et al. (2017). (b) Results of wavelet analyses for HYS-1 and TCDP-A. The *y*-axis represent the periodicity of orbital cycles, where *P* = precession (20-Kyr periodicity), *O* = obliquity (41-Kyr periodicity), *e* = short eccentricity (100-Kyr periodicity), and *E* = long eccentricity (405-Kyr periodicity). Blue and green colors indicate time intervals of poor correlation between the GR record and cycles of a specific periodicity, and red and yellow colors indicate intervals of strong correlation. (c) Astronomical solution of Earth's eccentricity and climatic precession and (d) obliquity indices for the studied time interval (Laskar et al., 2004) used for comparison with periodicities preserved in the sedimentary record as shown using wavelet analysis in (b). The black dashed line indicates the Miocene-Pliocene transition.

relatively constant since the late Pliocene (Hsieh et al., 2022; A. T. Lin et al., 2003; A. T. Lin & Watts, 2002; Nagel et al., 2013, 2014, 2018). At low latitudes, hydrological cycles such as the EASM and tropical cyclones are mainly driven by changes in insolation related to eccentricity-modulated precession (Clement et al., 2004; Gai et al., 2020; Merlis et al., 2013; Prell & Kutzbach, 1987; Tachikawa et al., 2011; Wang et al., 2017; Yamamoto et al., 2013). While strong precession signals are evident in EASM records from the Chinese Loess Plateau (e.g., Ao et al., 2016, 2021; Sun et al., 2010; S. Yang et al., 2018), they are generally not preserved in marine records from the South China Sea (Ao et al., 2011, 2016, 2021; Gai et al., 2020; Holbourn et al., 2021; Huybers, 2006; Li & Wang, 2015; Shi et al., 2022; Wang et al., 2017; Zhang et al., 2022). However, in shallow-marine environments, the completeness of the sedimentary record improves with increasing sedimentation rate and basin accommodation space, which result in enhanced preservation potential of precession signals (Figure 6e).

During the early stages of Taiwan orogenesis (prior to ca. 5.4 Ma, sedimentation rates and basin accommodation space were low because (a) there was no proximal sediment source (i.e., Taiwan), and (b) basin subsidence was low (Figures 3c and 6f; Nagel et al., 2018). Additionally, the sea along the southeast margin of Eurasia was open to the Pacific Ocean, exposing the shelf and shoreface to extensive wave reworking modulated by eustatic sea

**Figure 6.**

level change, the latter of which is driven by obliquity pacing of Antarctic Ice Sheet growth and decay. With the onset of deposition of the Shihliufen Shale (5.4–4.92 Ma), the foreland basin subsidence rate began to accelerate, and sediment flux from Taiwan began to increase (Figure 6f; Hsieh et al., 2022; Nagel et al., 2018). After

4.92 Ma, continued rapid uplift and erosion of the Taiwan orogen resulted in further subsidence of the WFB, increased sediment flux from land to sea, and the formation of the Taiwan Strait Figure 6f; Hsieh et al., 2022; Nagel et al., 2018). Enhanced currents (i.e., alongshore currents) resulted from the formation of the Taiwan Strait and the restriction and acceleration of water that flowed along the shelf. However, the semi-sheltered strait also limited the degree of sediment reworking by erosive wave processes in shallow water (e.g., Dashtgard et al., 2020) that truncated higher-frequency climate signals such as precession.

Sediment reworking by large waves is common in open, shallow-marine environments (Dashtgard et al., 2012; Myrow & Southard, 1996), such as the WFB before the Taiwan orogen fully emerged, and this typically decreases the temporal completeness of the sedimentary record. In particular, higher-frequency cycles such as precession are more susceptible to removal by sediment reworking, while lower-frequency cycles, such as eccentricity, have higher preservation potential. Neither obliquity nor precession are very clearly expressed in the record although they are significantly present (Figure S5 in Supporting Information S1). Because testing for amplitude relationships requires a dominant signal of precession or obliquity to be tested (Shackleton et al., 1995; Zeeden et al., 2015, 2019), the obliquity and eccentricity-modulated precession amplitudes in the GR datasets differ from astronomical solutions of orbital indices (Laskar et al., 2004; Figure 4). However, similar trends between the GR datasets and the $\delta^{18}O$ record suggest that an astronomical imprint exists in both locations (Figures 3a and 3b). The trends in sedimentation rates are also similar at both locations, which indicate that the tuning between the two locations is consistent (Figure 3c).

The open-ocean conditions in the pre-Taiwan Strait prior to 5.4 Ma resulted in the obscuration of precession-driven hydrological processes in the sedimentary system despite strong and highly variable orbital precession and an intensification of the EASM between ca. 8 and 3 Ma (e.g., Ao et al., 2016; Filippelli, 1997; Gai et al., 2020; Holbourn et al., 2021; Hui et al., 2021; Wan et al., 2006; Wang et al., 2005). The preservation of lower-frequency cycles is manifested in the HYS-1 record between 6.27 and 5.4 Ma, where distinct 100-Kyr signals occur throughout (Figures 5b and 6d). The 100-Kyr signals reflect the dynamic response of the EASM and related runoff to eccentricity modulation of summer insolation (Ao et al., 2021; Clemens & Tiedemann, 1997; Li & Wang, 2015; Wang et al., 2017).

The acceleration of foreland basin subsidence rate from 5.4 to 4.92 Ma resulted in increased water depths (>35 m; Dashtgard et al., 2020) and lower sedimentation rates at the paleogeographic positions of HYS-1 and TCDP-A. Despite increasing basin subsidence, the preservation of orbital oscillations is low through the Shihliufen Shale, and this is attributed to either (a) low sedimentation rates at deeper water depths resulting in cycles being below the resolution of the recording instrument; (b) low sedimentation rates at deeper water depths obscuring variations in sediment input; and/or (c) cycles not being visible in the GR proxy record due to a lack of contrasting lithology.

After 4.92 Ma, continued uplift of the Taiwan orogen resulted in further subsidence of the WFB and the formation of a strait that was semi-sheltered from the Pacific Ocean. As rapid uplift and erosion of the Taiwan orogen continued in the early Pliocene, it became the dominant sediment source to the WFB (Dashtgard et al., 2021; Hsieh et al., 2022). Sediment flux from the Taiwan orogen was likely higher after 4.92 Ma, although estimated sedimentation rates through the Yutengping Sandstone are comparable to the Kuantaoshan Sandstone in HYS-1 (Figure 3c) even with increased basin subsidence during deposition of the Yutengping Sandstone (Nagel et al., 2018). This is likely a consequence of sediment remobilization toward the South and East China Seas by alongshore currents that developed with the formation of the Taiwan Strait (Milliman et al., 2007; Nagel et al., 2018; Vaucher, Dillinger, et al., 2023). The combination of the formation of a semi-sheltered strait and increased basin accommodation space and sediment flux resulted in enhanced preservation of precession-driven EASM and tropical cyclone variability in the GR datasets after 4.92 Ma (Figure 6e).

Through the Yutengping Sandstone, the GR data in both HYS-1 and TCDP-A show overall strong eccentricity patterns with moderate obliquity. Precession is more variable between the two locations (Figure 6). At HYS-1,

**Figure 6.** (a) Astronomical solution of Earth's obliquity index for the studied time interval (Laskar et al., 2004). (b) Tuned GR datasets (HYS-1 in pink, TCDP-A in yellow) filtered using the Taner bandpass filter for obliquity (41-Kyr periodicity). The brown lines represent the amplitude (i.e., strength) of obliquity signal preserved in the GR record after applying the bandpass filter. The dashed black line represents the upper envelope of the filtered signal, which highlights peaks that correspond to strong obliquity signals preserved in the GR record. (c) Astronomical solution of Earths' eccentricity and climatic precession indices for the studied time interval (Laskar et al., 2004). (d) Tuned GR datasets filtered for short eccentricity (100-Kyr periodicity) and (e) precession (20-Kyr periodicity). (f) Western Foreland Basin subsidence over time at Dahan River (orange), Tsaohu River (green), and Chuhuangkeng (yellow) (from Nagel et al., 2013). These values are used to calculate basin subsidence, and the positions of these sections are shown in Figure 1.

20-Kyr amplitudes are strongest during eccentricity minima at ca. 4.8, 4.4, and 3.6 Ma, while in TCDP-A, peaks in precession amplitudes generally correspond to eccentricity maxima throughout the entire record (Figures 6c and 6e). The differences in precession signals preserved at HYS-1 and TCDP-A and their formation thicknesses may be a result of their positions relative to the Taiwan Strait. The present-day location of TCDP-A is farther inland from the Taiwan Strait than HYS-1. During the early Pliocene, it is likely that HYS-1 was in a more central position in the paleo-Taiwan Strait, which probably resulted in increased remobilization of sediment by alongshore currents from the region around HYS-1 toward the South and East China Seas. After 4.2 Ma, with continued uplift and western propagation of the Taiwan orogen, the depocenter at HYS-1 shifted from the center of the strait toward Taiwan. At TCDP-A, where sedimentation occurred more proximal to the Taiwan orogen and away from the stronger alongshore currents in the middle of the paleo-Taiwan Strait, the 20-Kyr cycles clearly reflect variations in eccentricity-modulated precession amplitude throughout the entire interval.

## 6. Conclusion

Traditionally, climate reconstructions for the late Miocene-Pliocene have emphasized the influence of 41-Kyr obliquity cycles on global climate because the obliquity signal is preserved in many climate archives from this time period (Clement et al., 2004; Naish et al., 2009; Patterson et al., 2014; Westerhold et al., 2020). However, climate of mid-to low-latitude regions is largely controlled by summer insolation paced by eccentricity-modulated precession, and there is evidence for this in EASM records from the Chinese Loess Plateau (e.g., Ao et al., 2016, 2021; Sun et al., 2010; S. Yang et al., 2018) and some shallow-marine sedimentary archives (e.g., Berger et al., 2006; Clement et al., 2004; Gai et al., 2020; Kutzbach, 1981; Prell & Kutzbach, 1987; Tachikawa et al., 2011; Wang et al., 2017; Yamamoto et al., 2013). This study shows that the orbital imprint on the shallow-marine realm is dependent on both the global climate state and the local depositional system, including sediment availability and basin accommodation space. The Taiwan Western Foreland Basin (WFB) provides an example of how a rapidly uplifting orogen can modify the expression of orbital cycles preserved in shallow-marine sedimentary archives at different stages of orogenesis.

The changes in orbital climate drivers preserved in the Kueichulin Formation reflect different stages of Taiwan orogenesis. During the early stages of Taiwan orogenesis, prior to 5.4 Ma, the Taiwan Strait did not exist, and sediment in the early WFB were susceptible to reworking by wave processes in the open Pacific Ocean. These large and energetic waves obscured or obliterated evidence in the sedimentary record of hydrological cycles driven by eccentricity-modulated precession. Consequently, in the Kuantaoshan Sandstone and prior to 5.4 Ma, there is weak preservation of precession signals as high-frequency oscillations are more prone to removal, while lower-frequency obliquity and eccentricity cycles remained. During the early stages of emergence of Taiwan (5.4–4.92 Ma), basin subsidence and water depths increased, but sedimentation rates remained low. These conditions resulted in poor preservation of orbital oscillations except for eccentricity maxima. After 4.92 Ma, the rapid uplift and erosion of the Taiwan orogen became the major sediment source to the WFB (Hsieh et al., 2022), and basin subsidence began to accelerate. Also, after 4.92 Ma, the emergence of the Taiwan orogen resulted in development of the Taiwan Strait which sheltered the WFB from the major erosive force of waves generated in the Pacific Ocean, especially during changes in eustatic sea level. The Taiwan orogen also became the dominant source of sediment to the WFB. The protection of the Taiwan Strait from Pacific Ocean waves and increased sediment flux led to enhanced preservation of precession signals.

## Conflict of Interest

The authors declare no conflicts of interest relevant to this study.

## Data Availability Statement

Additional information that supports the findings of this study, including the stratigraphic log of the Da'an River Kueichulin Fm outcrop, linear sedimentation rates, tie points used for astronomical tuning, and power spectrum of gamma-ray records are available as a part of the Supporting Information S1. Gamma-ray and magnetobiostratigraphic data used in this study, and the R script used for time-series and astrochronological analyses are available on PANGAEA (Hsieh et al., 2023).

## References

Ao, H., Dekkers, M. J., Qin, L., & Xiao, G. (2011). An updated astronomical timescale for the Plio-Pleistocene deposits from South China Sea and new insights into Asian monsoon evolution. *Quaternary Science Reviews*, *30*(13–14), 1560–1575. https://doi.org/10.1016/j.quascirev.2011.04.009

Ao, H., Roberts, A. P., Dekkers, M. J., Liu, X., Rohling, E. J., Shi, Z., et al. (2016). Late Miocene–Pliocene Asian monsoon intensification linked to Antarctic ice-sheet growth. *Earth and Planetary Science Letters*, *444*, 75–87. https://doi.org/10.1016/j.epsl.2016.03.028

Ao, H., Rohling, E. J., Zhang, R., Roberts, A. P., Holbourn, A. E., Ladant, J.-P., et al. (2021). Global warming-induced Asian hydrological climate transition across the Miocene–Pliocene boundary. *Nature Communications*, *12*(1), 6935. https://doi.org/10.1038/s41467-021-27054-5

Berger, A., Loutre, M. F., & Melice, J. L. (2006). Equatorial insolation: From precession harmonics to eccentricity frequencies. *Climate of the Past*, *2*, 131–136. https://doi.org/10.5194/cp-2-131-2006

Brady, N. C., & Weil, R. R. (2017). *The nature and properties of soils* (15th ed.). Pearson Education Ltd.

Burke, K. D., Williams, J. W., Chandler, M. A., Haywood, A. M., Lunt, D. J., & Otto-Bliesner, B. L. (2018). Pliocene and Eocene provide best analogs for near-future climates. *Proceedings of the National Academy of Sciences*, *115*(52), 13288–13293. https://doi.org/10.1073/pnas.1809600115

Castelltort, S., Nagel, S., Mouthereau, F., Lin, A. T., Wetzel, A., Kaus, B., et al. (2011). Sedimentology of early Pliocene sandstones in the south-western Taiwan foreland: Implications for basin physiography in the early stages of collision. *Journal of Asian Earth Sciences*, *40*(1), 52–71. https://doi.org/10.1016/j.jseaes.2010.09.005

Catuneanu, O. (2006). *Principles of sequence stratigraphy* (1st ed.). Elsevier.

Chang, S. S. L. (1971). Regional stratigraphy and petroleum possibilities of Miocene formations in northwestern Taiwan, China. *American Association of Petroleum Geologists Bulletin*, *55*(10), 1838–1865. https://doi.org/10.1306/819A3DAE-16C5-11D7-8645000102C1865D

Chang, S. S. L., & Chi, W. R. (1983). Neogene nanoplankton biostratigraphy in Taiwan and the tectonic implications. *Petroleum Geology of Taiwan*, *19*, 93–147.

Chen, C.-W., Oguchi, T., Hayakawa, Y. S., Saito, H., Chen, H., Lin, G.-W., et al. (2018). Sediment yield during typhoon events in relation to landslides, rainfall, and catchment areas in Taiwan. *Geomorphology*, *303*, 540–548. https://doi.org/10.1016/j.geomorph.2017.11.007

Chen, W.-S. (2016). *An introduction to the geology of Taiwan*. Geological Society of Taiwan.

Chou, J. T. (1972). A sedimentologic and paleogeographic study of the upper Cenozoic clastic sequences in the Chiayi region, western Taiwan. *Petroleum Geology of Taiwan*, *10*, 141–158.

Chou, Y.-W., & Yu, H.-S. (2002). Structural expressions of flexural extension in the arc-continent collisional foredeep of western Taiwan. *Special Papers - Geological Society of America*, *358*, 1–12. https://doi.org/10.1130/0-8137-2358-2.1

Clemens, S. C., & Tiedemann, R. (1997). Eccentricity forcing of Pliocene–Early Pleistocene climate revealed in a marine oxygen-isotope record. *Nature*, *385*(6619), 801–804. https://doi.org/10.1038/385801a0

Clement, A. C., Hall, A., & Broccoli, A. J. (2004). The importance of precessional signals in the tropical climate. *Climate Dynamics*, *22*(4), 327–341. https://doi.org/10.1007/s00382-003-0375-8

Coumou, D., & Rahmstorf, S. (2012). A decade of weather extremes. *Nature Climate Change*, *2*(7), 491–496. https://doi.org/10.1038/nclimate1452

Covey, M. (1986). The evolution of foreland basins to steady state: Evidence from the Western Taiwan Foreland Basin. In *Foreland basins* (pp. 77–90). Blackwell Publishing Ltd. https://doi.org/10.1002/9781444303810.ch4

Dadson, S. J., Hovius, N., Chen, H., Dade, W. B., Hsieh, M.-L., Willett, S. D., et al. (2003). Links between erosion, runoff variability and seismicity in the Taiwan orogen. *Nature*, *426*(6967), 648–651. https://doi.org/10.1038/nature02150

Dadson, S. J., Hovius, N., Chen, H., Dade, W. B., Lin, J.-C., Hsu, M.-L., et al. (2004). Earthquake-triggered increase in sediment delivery from an active mountain belt. *Geology*, *32*(8), 733. https://doi.org/10.1130/G20639.1

Dashtgard, S. E., Löwemark, L., Vaucher, R., Pan, Y.-Y., Pilarczyk, J. E., & Castelltort, S. (2020). Tropical cyclone deposits in the Pliocene Taiwan Strait: Processes, examples, and conceptual model. *Sedimentary Geology*, *405*, 105687. https://doi.org/10.1016/j.sedgeo.2020.105687

Dashtgard, S. E., Löwemark, L., Wang, P.-L., Setiaji, R. A., & Vaucher, R. (2021). Geochemical evidence of tropical cyclone controls on shallow-marine sedimentation (Pliocene, Taiwan). *Geology*, *49*(5), 566–570. https://doi.org/10.1130/G48586.1

Dashtgard, S. E., MacEachern, J. A., Frey, S. E., & Gingras, M. K. (2012). Tidal effects on the shoreface: Towards a conceptual framework. *Sedimentary Geology*, *279*, 42–61. https://doi.org/10.1016/j.sedgeo.2010.09.006

Dekens, P. S., Ravelo, A. C., & McCarthy, M. D. (2007). Warm upwelling regions in the Pliocene warm period. *Paleoceanography*, *22*(3), PA3211. https://doi.org/10.1029/2006PA001394

Dolan, A. M., Haywood, A. M., Hill, D. J., Dowsett, H. J., Hunter, S. J., Lunt, D. J., & Pickering, S. J. (2011). Sensitivity of Pliocene ice sheets to orbital forcing. *Palaeogeography, Palaeoclimatology, Palaeoecology*, *309*(1), 98–110. https://doi.org/10.1016/j.palaeo.2011.03.030

Dowsett, H. J., & Cronin, T. M. (1990). High eustatic sea level during the middle Pliocene: Evidence from the southeastern U.S. Atlantic Coastal Plain. *Geology*, *18*(5), 435–438. https://doi.org/10.1130/0091-7613(1990)018<0435:HESLDT>2.3.CO;2

Dowsett, H. J., Robinson, M. M., Haywood, A. M., Hill, D. J., Dolan, A. M., Stoll, D. K., et al. (2012). Assessing confidence in Pliocene sea surface temperatures to evaluate predictive models. *Nature Climate Change*, *2*(5), 365–371. https://doi.org/10.1038/nclimate1455

Fedorov, A. V., Brierley, C. M., & Emanuel, K. (2010). Tropical cyclones and permanent El Niño in the early Pliocene epoch. *Nature*, *463*(7284), 1066–1070. https://doi.org/10.1038/nature08831

Fedorov, A. V., Brierley, C. M., Lawrence, K. T., Liu, Z., Dekens, P. S., & Ravelo, A. C. (2013). Patterns and mechanisms of early Pliocene warmth. *Nature*, *496*(7443), 43–49. https://doi.org/10.1038/nature12003

Fedorov, A. V., Dekens, P. S., McCarthy, M., Ravelo, A. C., de Menocal, P. B., Barreiro, M., et al. (2006). The Pliocene paradox (Mechanisms for a permanent El Niño). *Science*, *312*(5779), 1485–1489. https://doi.org/10.1126/science.1122666

Filippelli, G. M. (1997). Intensification of the Asian monsoon and a chemical weathering event in the late Miocene–early Pliocene: Implications for late Neogene climate change. *Geology*, *25*(1), 27–30. https://doi.org/10.1130/0091-7613(1997)025<0027:IOTAMA>2.3.CO;2

Gai, C., Liu, Q., Roberts, A. P., Chou, Y., Zhao, X., Jiang, Z., & Liu, J. (2020). East Asian monsoon evolution since the late Miocene from the South China Sea. *Earth and Planetary Science Letters*, *530*, 115960. https://doi.org/10.1016/j.epsl.2019.115960

Gouhier, T. C., Grinsted, A., & Simko, V. (2018). R package biwavelet: Conduct univariate and bivariate wavelet analyses (version 0.20.17). Retrieved from https://github.com/tgouhier/biwavelet

Grant, G. R., Naish, T. R., Dunbar, G. B., Stocchi, P., Kominz, M. A., Kamp, P. J. J., et al. (2019). The amplitude and origin of sea-level variability during the Pliocene epoch. *Nature*, *574*(7777), 237–241. https://doi.org/10.1038/s41586-019-1619-z

Green, W. G., & Fearon, R. E. (1940). Well logging by radioactivity. *Geophysics*, *5*(3), 272–283. https://doi.org/10.1190/1.1441810

Haywood, A. M., Hill, D. J., Dolan, A. M., Otto-Bliesner, B. L., Bragg, F., Chan, W.-L., et al. (2013). Large-scale features of Pliocene climate: Results from the Pliocene model intercomparison project. *Climate of the Past*, *9*(1), 191–209. https://doi.org/10.5194/cp-9-191-2013

Haywood, A. M., & Valdes, P. J. (2004). Modelling Pliocene warmth: Contribution of atmosphere, oceans and cryosphere. *Earth and Planetary Science Letters*, *218*(3), 363–377. https://doi.org/10.1016/S0012-821X(03)00685-X

Hill, D. J., Dolan, A. M., Haywood, A. M., Hunter, S. J., & Stoll, D. K. (2010). Sensitivity of the Greenland Ice Sheet to Pliocene sea surface temperatures. *Stratigraphy*, *7*(2–3), 111–121.

Holbourn, A. E., Kuhnt, W., Clemens, S. C., & Heslop, D. (2021). A ~12 Myr Miocene record of East Asian monsoon variability from the South China Sea. *Paleoceanography and Paleoclimatology*, *36*(7), e2021PA004267. https://doi.org/10.1029/2021PA004267

Horng, C. S., & Shea, K. S. (2007). The Quaternary magnetobiostratigraphy of Taiwan and Penglai orogenic events. *Special Publication of the Central Geological Survey*, *18*, 51–83.

Hsieh, A. I., Dashtgard, S. E., Wang, P.-L., Horng, C.-S., Su, C.-C., Lin, A. T., et al. (2022). Multi-proxy evidence for rapidly shifting sediment sources to the Taiwan Western Foreland Basin at the Miocene-Pliocene transition. *Basin Research*, *00*(3), 1–17. https://doi.org/10.1111/bre.12741

Hsieh, A. I., Vaucher, R., Löwemark, L., Dashtgard, S. E., Lin, A. T., Horng, C.-S., & Zeeden, C. (2023). Time-series analysis of gamma-ray records through the late Miocene–Pliocene Kueichulin Formation from the Taiwan Western Foreland Basin. [Dataset]. PANGAEA. https://doi.org/10.1594/PANGAEA.958492

Huang, T.-C. (1976). Neogene calcareous nannoplankton biostratigraphy viewed from the Chuhuangkeng section, northwestern Taiwan. *Proceedings of the Geological Society of China*, *19*, 7–24.

Hui, Z., Zhou, X., Chevalier, M., Wei, X., Pan, Y., & Chen, Y. (2021). Miocene East Asia summer monsoon precipitation variability and its possible driving forces. *Palaeogeography, Palaeoclimatology, Palaeoecology*, *581*, 110609. https://doi.org/10.1016/j.palaeo.2021.110609

Huybers, P. (2006). Early Pleistocene glacial cycles and the integrated summer insolation forcing. *Science*, *313*(5786), 508–511. https://doi.org/10.1126/science.1125249

Kao, S. J., & Milliman, J. D. (2008). Water and sediment discharge from small mountainous rivers, Taiwan: The roles of lithology, episodic events, and human activities. *The Journal of Geology*, *116*(5), 431–448. https://doi.org/10.1086/590921

Keeling, R. F., & Keeling, C. D. (2017). *Atmospheric monthly in situ CO₂ data-Mauna Loa Observatory*. Scripps CO₂ Program Data.

Kelman, I. (2013). Saffir–Simpson hurricane intensity scale. In P. T. Bobrowsky (Ed.), *Encyclopedia of natural hazards* (pp. 882–883). Springer. https://doi.org/10.1007/978-1-4020-4399-4_306

Kossin, J. P. (2018). A global slowdown of tropical-cyclone translation speed. *Nature*, *558*(7708), 104–107. https://doi.org/10.1038/s41586-018-0158-3

Kossin, J. P., Knapp, K. R., Olander, T. L., & Velden, C. S. (2020). Global increase in major tropical cyclone exceedance probability over the past four decades. *Proceedings of the National Academy of Sciences - PNAS*, *117*(22), 11975–11980. https://doi.org/10.1073/pnas.1920849117

Kutzbach, J. E. (1981). Monsoon climate of the early holocene: Climate experiment with the Earth's orbital parameters for 9000 years ago. *Science*, *214*(4516), 59–61. https://doi.org/10.1126/science.214.4516.59

Laskar, J., Robutel, P., Joutel, F., Gastineau, M., Correia, A. C. M., & Levrard, B. (2004). A long-term numerical solution for the insolation quantities of the Earth. *Astronomy & Astrophysics*, *428*(1), 261–285. https://doi.org/10.1051/0004-6361:20041335

Li, J., & Wang, P. (2015). Long eccentricity cycle in Pliocene oceanic carbon reservoir: A comparison between the Mediterranean and the South China Sea. *Deep Sea Research Part II: Topical Studies in Oceanography*, *122*, 163–171. https://doi.org/10.1016/j.dsr2.2015.02.004

Lin, A. T., Wang, S.-M., Hung, J.-H., Wu, M.-S., & Liu, C.-S. (2007). Lithostratigraphy of the Taiwan Chelungpu-Fault drilling project-A borehole and its neighboring region, Central Taiwan. *Terrestrial, Atmospheric and Oceanic Sciences*, *18*(2), 223. https://doi.org/10.3319/TAO.2007.18.2.223(TCDP

Lin, A. T., & Watts, A. B. (2002). Origin of the West Taiwan basin by orogenic loading and flexure of a rifted continental margin. *Journal of Geophysical Research*, *107*(B9), ETG2-1–ETG2-19. https://doi.org/10.1029/2001JB000669

Lin, A. T., Watts, A. B., & Hesselbo, S. P. (2003). Cenozoic stratigraphy and subsidence history of the South China Sea margin in the Taiwan region: Cenozoic stratigraphy of Taiwan. *Basin Research*, *15*(4), 453–478. https://doi.org/10.1046/j.1365-2117.2003.00215.x

Lin, C.-W., & Chen, W.-S. (2016). *Geologic map of Taiwan*. Geological Society of Taiwan.

Lunt, D. J., Foster, G. L., Haywood, A. M., & Stone, E. J. (2008). Late Pliocene Greenland glaciation controlled by a decline in atmospheric CO₂ levels. *Nature*, *454*(7208), 1102–1105. https://doi.org/10.1038/nature07223

Lurcock, P. C., & Wilson, G. S. (2012). PuffinPlot: A versatile, user-friendly program for paleomagnetic analysis. *Geochemistry, Geophysics, Geosystems*, *13*(6), Q06Z45. https://doi.org/10.1029/2012GC004098

Martini, E. (1971). Standard tertiary and quaternary calcareous nannoplankton zonation. In A. Farinacci (Ed.), *Proceedings of the Second International conference on planktonic microfossils* (Vol. 2, pp. 739–785).

Merlis, T. M., Schneider, T., Bordoni, S., & Eisenman, I. (2013). The tropical precipitation response to orbital precession. *Journal of Climate*, *26*(6), 2010–2021. https://doi.org/10.1175/JCLI-D-12-00186.1

Meyers, S. R. (2012). Seeing red in cyclic stratigraphy: Spectral noise estimation for astrochronology. *Paleoceanography*, *27*(3), PA3228. https://doi.org/10.1029/2012PA002307

Meyers, S. R. (2014). Astrochron: An R package for astrochronology. Retrieved from https://cran.r-project.org/package=astrochron

Miller, K. G., Wright, J. D., Browning, J. V., Kulpecz, A., Kominz, M., Naish, T. R., et al. (2012). High tide of the warm Pliocene; implications of global sea level for Antarctic deglaciation. *Geology*, *40*(5), 407–410. https://doi.org/10.1130/G32869.1

Milliman, J. D., & Kao, S. (2005). Hyperpycnal discharge of fluvial sediment to the ocean: Impact of Super-Typhoon Herb (1996) on Taiwanese Rivers. *The Journal of Geology*, *113*(5), 503–516. https://doi.org/10.1086/431906

Milliman, J. D., Lee, T. Y., Huang, J. C., & Kao, S. J. (2017). Impact of catastrophic events on small mountainous rivers: Temporal and spatial variations in suspended- and dissolved-solid fluxes along the Choshui River, central western Taiwan, during Typhoon Mindulle, July 2–6, 2004. *Geochimica et Cosmochimica Acta*, *205*, 272–294. https://doi.org/10.1016/j.gca.2017.02.015

Milliman, J. D., Lin, S. W., Kao, S. J., Liu, J. P., Liu, C. S., Chiu, J. K., & Lin, Y. C. (2007). Short-term changes in seafloor character due to flood-derived hyperpycnal discharge: Typhoon Mindulle, Taiwan, July 2004. *Geology*, *35*(9), 779–782. https://doi.org/10.1130/G23760A.1

Myrow, P. M., & Southard, J. B. (1996). Tempestite deposition. *Journal of Sedimentary Research*, *66*, 875–887. https://doi.org/10.1306/D426842D-2B26-11D7-8648000102C1865D

Nagel, S., Castelltort, S., Garzanti, E., Lin, A. T., Willett, S. D., Mouthereau, F., et al. (2014). Provenance evolution during arc-continent collision: Sedimentary petrography of Miocene to Pleistocene sediments in the Western Foreland Basin of Taiwan. *Journal of Sedimentary Research*, *84*(7), 513–528. https://doi.org/10.2110/jsr.2014.44

Nagel, S., Castelltort, S., Wetzel, A., Willett, S. D., Mouthereau, F., & Lin, A. T. (2013). Sedimentology and foreland basin paleogeography during Taiwan arc continent collision. *Journal of Asian Earth Sciences*, *62*, 180–204. https://doi.org/10.1016/j.jseaes.2012.09.001

Nagel, S., Granjeon, D., Willett, S., Lin, A. T., & Castelltort, S. (2018). Stratigraphic modeling of the Western Taiwan foreland basin: Sediment flux from a growing mountain range and tectonic implications. *Marine and Petroleum Geology*, *96*, 331–347. https://doi.org/10.1016/j.marpetgeo.2018.05.034

Naish, T., Powell, R., Levy, R., Wilson, G., Scherer, R., Talarico, F., et al. (2009). Obliquity-paced Pliocene West Antarctic ice sheet oscillations. *Nature*, *458*(7236), 322–328. https://doi.org/10.1038/nature07867

Ogg, J. G. (2020). Chapter 5 - Geomagnetic polarity time scale. In F. M. Gradstein, J. G. Ogg, M. D. Schmitz, & G. M. Ogg (Eds.), *Geologic time scale 2020* (pp. 159–192). Elsevier. https://doi.org/10.1016/B978-0-12-824360-2.00005-X

Pan, T.-Y., Lin, A. T., & Chi, W.-R. (2015). Paleoenvironments of the evolving Pliocene to early Pleistocene foreland basin in northwestern Taiwan: An example from the Dahan River section: Paleoenvironments of NW Taiwan foreland. *Island Arc*, *24*(3), 317–341. https://doi.org/10.1111/iar.12113

Patterson, M. O., McKay, R., Naish, T., Escutia, C., Jimenez-Espejo, F. J., Raymo, M. E., et al. (2014). Orbital forcing of the East Antarctic ice sheet during the Pliocene and early Pleistocene. *Nature Geoscience*, *7*(11), 841–847. https://doi.org/10.1038/ngeo2273

Pollard, D., & DeConto, R. M. (2009). Modelling West Antarctic ice sheet growth and collapse through the past five million years. *Nature*, *458*(7236), 329–332. https://doi.org/10.1038/nature07809

Prell, W. L., & Kutzbach, J. E. (1987). Monsoon variability over the past 150,000 years. *Journal of Geophysical Research*, *92*(D7), 8411. https://doi.org/10.1029/JD092iD07p08411

Raffi, I., Backman, J., Fornaciari, E., Pälike, H., Rio, D., Lourens, L., & Hilgen, F. (2006). A review of calcareous nannofossil astrobiochronology encompassing the past 25 million years. *Quaternary Science Reviews*, *25*(23–24), 3113–3137. https://doi.org/10.1016/j.quascirev.2006.07.007

Raffi, I., Wade, B. S., Pälike, H., Beu, A. G., Cooper, R., Crundwell, M. P., et al. (2020). Chapter 29 - The Neogene period. In F. M. Gradstein, J. G. Ogg, M. D. Schmitz, & G. M. Ogg (Eds.), *Geologic time scale 2020* (pp. 1141–1215). Elsevier. https://doi.org/10.1016/B978-0-12-824360-2.00029-2

Raymo, M. E., & Horowitz, M. (1996). Organic carbon paleo-pCO$_2$ and marine-ice core correlations and chronology. *Geophysical Research Letters*, *23*(4), 367–370. https://doi.org/10.1029/96GL00254

R Core Team. (2022). *R: A language and environment for statistical computing*. R Foundation for Statistical Computing. Retrieved from https://www.R-project.org/

Savin, S. M., Douglas, R. G., & Stehli, F. G. (1975). Tertiary marine paleotemperatures. *GSA Bulletin*, *86*(11), 1499–1510. https://doi.org/10.1130/0016-7606(1975)86<1499:Tmp>2.0.Co;2

Schlumberger (1989). *Log interpretation principles/applications*. Schlumberger.

Shackleton, N., Hagelberg, T., & Crowhurst, S. (1995). Evaluating the success of astronomical tuning: Pitfalls of using coherence as a criterion for assessing pre-Pleistocene timescales. *Paleoceanography*, *10*(4), 693–697. https://doi.org/10.1029/95PA01454

Shaw, C.-L. (1996). Stratigraphic correlation and isopach maps of the Western Taiwan Basin. *Terrestrial, Atmospheric and Oceanic Sciences*, *7*(3), 333–360. https://doi.org/10.3319/TAO.1996.7.3.333(T)

Shea, K.-S., & Huang, T. (2003). Tertiary stratigraphy in Taiwan. *The Taiwan Mining Industry*, *55*, 17–32.

Shi, M., Wu, H., Ferré, E. C., Satolli, S., Fang, Q., Nie, Y., et al. (2022). Middle Miocene-Pleistocene Magneto-Cyclostratigraphy from IODP Site U1501 in the Northern South China Sea. *Frontiers of Earth Science*, *10*, 882617. https://doi.org/10.3389/feart.2022.882617

Simoes, M., & Avouac, J. P. (2006). Investigating the kinematics of mountain building in Taiwan from the spatiotemporal evolution of the foreland basin and western foothills. *Journal of Geophysical Research*, *111*(B10), B10401. https://doi.org/10.1029/2005JB004209

Singer, A. (1980). The paleoclimatic interpretation of clay minerals in soils and weathering profiles. *Earth-Science Reviews*, *15*(4), 303–326. https://doi.org/10.1016/0012-8252(80)90113-0

Steer, P., Jeandet, L., Cubas, N., Marc, O., Meunier, P., Simoes, M., et al. (2020). Earthquake statistics changed by typhoon-driven erosion. *Scientific Reports*, *10*(1), 10899. https://doi.org/10.1038/s41598-020-67865-y

Sun, Y., An, Z., Clemens, S. C., Bloemendal, J., & Vandenberghe, J. (2010). Seven million years of wind and precipitation variability on the Chinese Loess Plateau. *Earth and Planetary Science Letters*, *297*(3–4), 525–535. https://doi.org/10.1016/j.epsl.2010.07.004

Tachikawa, K., Cartapanis, O., Vidal, L., Beaufort, L., Barlyaeva, T., & Bard, E. (2011). The precession phase of hydrological variability in the Western Pacific Warm Pool during the past 400 ka. *Quaternary Science Reviews*, *30*(25–26), 3716–3727. https://doi.org/10.1016/j.quascirev.2011.09.016

Taner, M. T. (1992). *Attributes revisited (Technical report)*. Rock Solid Images, Inc. Retrieved from http://www.rocksolidimages.com/pdf/attrib_revisited.htm#_Toc328470897

Teng, L. S. (1990). Geotectonic evolution of late Cenozoic arc-continent collision in Taiwan. *Tectonophysics*, *183*(1–4), 57–76. https://doi.org/10.1016/0040-1951(90)90188-E

Teng, L. S., Wang, Y., Tang, C.-H., Huang, C.-Y., Huang, T.-C., Yu, M.-S., & Ke, A. (1991). Tectonic aspects of the Paleogene depositional basin of northern Taiwan. *Proceedings of the Geology Society of China*, *34*, 313–336.

Thomson, D. J. (1982). Spectrum estimation and harmonic analysis. *Proceedings of the IEEE*, *70*(9), 1055–1096. https://doi.org/10.1109/PROC.1982.12433

Tierney, J. E., Haywood, A. M., Feng, R., Bhattacharya, T., & Otto-Bliesner, B. L. (2019). Pliocene warmth consistent with greenhouse gas forcing. *Geophysical Research Letters*, *46*(15), 9136–9144. https://doi.org/10.1029/2019GL083802

Vaucher, R., Dashtgard, S. E., Horng, C.-S., Zeeden, C., Dillinger, A., Pan, Y.-Y., et al. (2021). Insolation-paced sea level and sediment flux during the early Pleistocene in Southeast Asia. *Scientific Reports*, *11*(1), 16707. https://doi.org/10.1038/s41598-021-96372-x

Vaucher, R., Dillinger, A., Hsieh, A. I., Chi, W.-R., Löwemark, L., & Dashtgard, S. E. (2023). *Storm-flood-dominated delta succession in the Pleistocene Taiwan Strait*. The Depositional Record.

Vaucher, R., Zeeden, C., Hsieh, A. I., Kaboth-Bahr, S., Lin, A. T., Horng, C.-S., & Dashtgard, S. E. (2023). Hydroclimate dynamics during the Plio-Pleistocene transition in the northwest Pacific realm. *Global and Planetary Change*, *223*, 104088. https://doi.org/10.1016/j.gloplacha.2023.104088

Wan, S., Li, A., Clift, P. D., & Jiang, H. (2006). Development of the East Asian summer monsoon: Evidence from the sediment record in the South China Sea since 8.5 Ma. *Palaeogeography, Palaeoclimatology, Palaeoecology*, *241*(1), 139–159. https://doi.org/10.1016/j.palaeo.2006.06.013

Wang, P. X., Clemens, S., Beaufort, L., Braconnot, P., Ganssen, G., Jian, Z., et al. (2005). Evolution and variability of the Asian monsoon system: State of the art and outstanding issues. *Quaternary Science Reviews*, *24*(5–6), 595–629. https://doi.org/10.1016/j.quascirev.2004.10.002

Wang, P. X., Wang, B., Cheng, H., Fasullo, J., Guo, Z., Kiefer, T., & Liu, Z. (2017). The global monsoon across time scales: Mechanisms and outstanding issues. *Earth-Science Reviews*, *174*, 84–121. https://doi.org/10.1016/j.earscirev.2017.07.006

Wara, M. W., Ravelo, A. C., & Delaney, M. L. (2005). Permanent El Niño-like conditions during the Pliocene warm period. *Science*, *309*(5735), 758–761. https://doi.org/10.1126/science.1112596

Westerhold, T., Marwan, N., Drury, A. J., Liebrand, D., Agnini, C., Anagnostou, E., et al. (2020). An astronomically dated record of Earth's climate and its predictability over the last 66 million years. *Science*, *369*(6509), 1383–1387. https://doi.org/10.1126/science.aba6853

Wilkens, R. H., Westerhold, T., Drury, A. J., Lyle, M., Gorgas, T., & Tian, J. (2017). Revisiting the Ceara Rise, equatorial Atlantic Ocean: Isotope stratigraphy of ODP Leg 154 from 0 to 5 Ma. *Climate of the Past*, *13*(7), 779–793. https://doi.org/10.5194/cp-13-779-2017

Yamamoto, M., Sai, H., Chen, M.-T., & Zhao, M. (2013). The East Asian winter monsoon variability in response to precession during the past 150 000 yr. *Climate of the Past*, *9*(6), 2777–2788. https://doi.org/10.5194/cp-9-2777-2013

Yan, Q., Wei, T., Korty, R. L., Kossin, J. P., Zhang, Z., & Wang, H. (2016). Enhanced intensity of global tropical cyclones during the mid-Pliocene warm period. *Proceedings of the National Academy of Sciences*, *113*(46), 12963–12967. https://doi.org/10.1073/pnas.1608950113

Yang, S., Ding, Z., Feng, S., Jiang, W., Huang, X., & Guo, L. (2018). A strengthened East Asian Summer Monsoon during Pliocene warmth: Evidence from 'red clay' sediments at Pianguan, northern China. *Journal of Asian Earth Sciences*, *155*, 124–133. https://doi.org/10.1016/j.jseaes.2017.10.020

Yang, Y., Piper, D. J. W., Normandeau, A., Zhou, L., Jia, J., Wang, Y. P., & Gao, S. (2022). A late Holocene shift of typhoon activity recorded by coastal sedimentary archives in eastern China. *Sedimentology*, *69*(2), 954–969. https://doi.org/10.1111/sed.12934

Yu, H.-S., & Chou, Y.-W. (2001). Characteristics and development of the flexural forebulge and basal unconformity of Western Taiwan Foreland Basin. *Tectonophysics*, *333*(1–2), 277–291. https://doi.org/10.1016/S0040-1951(00)00279-1

Zeeden, C., Kaboth, S., Hilgen, F. J., & Laskar, J. (2018). Taner filter settings and automatic correlation optimisation for cyclostratigraphic studies. *Computers & Geosciences*, *119*, 18–28. https://doi.org/10.1016/j.cageo.2018.06.005

Zeeden, C., Meyers, S. R., Hilgen, F. J., Lourens, L. J., & Laskar, J. (2019). Time scale evaluation and the quantification of obliquity forcing. *Quaternary Science Reviews*, *209*, 100–113. https://doi.org/10.1016/j.quascirev.2019.01.018

Zeeden, C., Meyers, S. R., Lourens, L. J., & Hilgen, F. J. (2015). Testing astronomically tuned age models. *Paleoceanography*, *30*(4), 369–383. https://doi.org/10.1002/2014PA002762

Zhang, C., Yang, S., Huang, X., Dou, Y., Li, F., Xu, X., et al. (2022). Sea level change and Kuroshio intrusion dominated Taiwan sediment source-to-sink processes in the northeastern South China Sea over the past 244 kyrs. *Quaternary Science Reviews*, *287*, 107558. https://doi.org/10.1016/j.quascirev.2022.107558